

Research Article

Axial-Symmetry Numerical Approaches for Noise Predicting and Attenuating of Rifle Shooting with Suppressors

Shi-Wei Lo,¹ Chang-Hsien Tai,¹ and Jyh-Tong Teng²

¹ *Department of Vehicle Engineering, National Pingtung University of Science and Technology, Pingtung 91201, Taiwan*

² *Department of Mechanical Engineering, Chung Yuan Christian University, Chung-Li 32023, Taiwan*

Correspondence should be addressed to Jyh-Tong Teng, jtteng1@gmail.com

Received 16 January 2011; Accepted 1 August 2011

Academic Editor: Edward Swim

Copyright © 2011 Shi-Wei Lo et al. This is an open access article distributed under the Creative Commons Attribution License, which permits unrestricted use, distribution, and reproduction in any medium, provided the original work is properly cited.

The moving bullet out of a rifle barrel is propelled by a fired explosive charge. Subsequently, a disturbed muzzle blast wave is initiated which lasts several milliseconds. In this study, axially symmetric, unsteady, Large Eddy Simulation (LES), and Ffowcs Williams and Hawkins (FWH) equations were solved by the implicit-time formulation. For the spatial discretization, second order upwind scheme was employed. In addition, dynamic mesh model was used to where the ballistic domain changed with time due to the motion of bullet. Results obtained for muzzle flow field and for noise recorded were compared with those obtained from experimental data; these two batches of results were in agreement. Five cases of gunshot including one model of an unsuppressed rifle and four models of suppressors were simulated. Besides, serial images of species distributions and velocity vectors-pressure contours in suppressors and near muzzle field were displayed. The sound pressure levels (dB) in far field that were post-processed by the fast Fourier transform (FFT) were compared. The proposed physical model and the numerical simulations used in the present work are expected to be extended to solve other shooting weapon problems with three-dimensional and complex geometries.

1. Introduction

To a rifleman in the battlefield, especially to a sniper, acoustic attenuation in shooting is very important. In a rifle shooting, muzzle blast wave caused by the discharged gas is a main acoustic source, the main acoustic source for analyzing the impact of blast on the far field receivers. The associated chemical energy released rapidly from the propellant in a gun generates muzzle blast and flash phenomena in a few milliseconds. The sudden discharge is

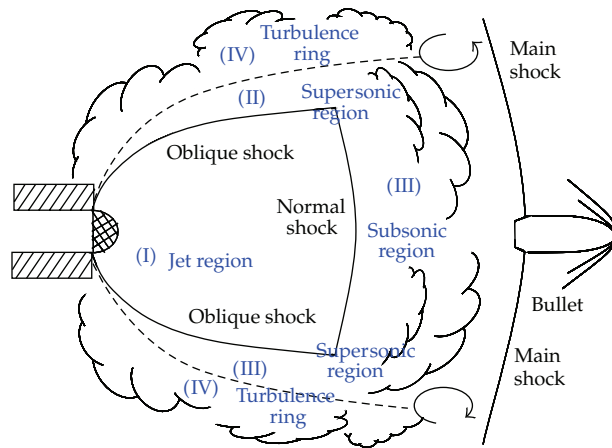


Figure 1: Schematic diagram of muzzle flow following a gunshot.

generally fuel-rich and mixes with air turbulently entrained from the surroundings [1]. While a bullet is passing through the muzzle, a main shock wave attached on the bullet is generated during its flight at supersonic velocity, as shown in Figure 1. The discharged propellant gas generates a normal wave and an oblique shock wave. Besides, the jet boundary is formed and it encloses the normal and oblique shock waves. Inside the region surrounded by the normal and oblique shock waves (region I), the flow velocity is supersonic. In region II, which is between oblique and jet boundaries, the flow is also supersonic. However, the velocity behind the main shock is subsonic and numerous vortices are formed in this area (region III). Out of jet boundary (region IV), turbulence rings are generated by the interaction of jet flow and surrounding air. The main shock and air disturbance in both regions III and IV are the acoustic sources which cause the receivers to hear about the noises [2, 3].

The supersonic projectile causes an acoustic shock wave that propagates away from the bullet's path. A shock wave expands as a cone behind the bullet, with the wave front propagating outward at the speed of sound [4, 5]. Impulse noise is a transient noise that arises as a result of a sudden release of energy into the atmosphere. The impulses are largely dependent upon the geometry and scale of the source. In order to trap the expanding gases that create the loud supersonic crack of a fired bullet, a sound suppressor is attached to the muzzle of a firearm. The installations of muzzle blast suppressors are to minimize the sound emanating from a rifle upon discharge, as shown in Figure 2, in order to avoid detection of the shooter by enemy forces [6, 7]. Thus, it is distinctly advantageous to have the sound emitted from a gunshot to be as quiet as possible. Suppressors most commonly use a series of baffles in a tube surrounding an extension of the bore that forces the gases to expend their energy in a contained space. Substantial effort had been devoted to understanding the mechanism of muzzle flow fields [8, 9]. Hudson et al. [10] designed a suppressor to compare the experimentally obtained results in the literature with those obtained by CFD methodology for the sound mitigation of gunshot. As a practical rule, the impulse noise of small caliber weapons is concentrated in the frequency range of 500–1000 Hz while that of large caliber weapons and explosions is in the low-frequency range of less than 200 Hz [11]. Many researches dedicated to studying the design of suppressors to attenuate noise by changing the frequency of gunshot noise [12–14].

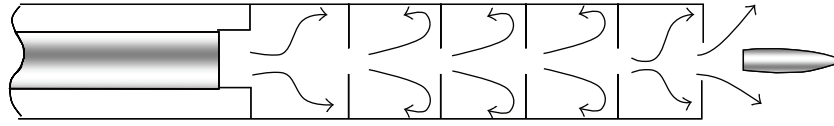


Figure 2: Schematic illustration of muzzle silencer during a gunshot.

In fact, sounds have much lower energy than fluid flows. It is a great challenge to predict each flow phenomenon and to simulate sound waves numerically. In recent years, a variety of approaches were used, including direct method [15, 16] used in near field, integral method employed in near field, and a broadband-noise-source-models method [17, 18] quantifying the local contribution to the total acoustic power generated by the flow. Moreover, integral method calculates the near-field flow obtained from appropriate unsteady turbulence governing equations to predict the sound with the aid of analytically derived integral solutions to wave equations [19, 20]. The corresponding sound field has been obtained with help of the Lighthill equation [21].

A gunshot generates complex physical phenomena in muzzle flow, which involve chemical reactions induced by the burning gases and transient interaction between shock waves and jet flow. Since the disturbances of muzzle flow are the main sources to calculate the acoustics at far field receivers, the species gases in chamber and the large Eddy simulation (LES) were considered in this study. The present numerical methodology utilized the cell-averaged finite volume method. Five gunshot cases including a rifle without suppressor and others equipped with an acoustical suppressor were simulated and compared; generations of noise by blast waves during the shooting process were analyzed. The purpose was to optimize the design of noise attenuation. Axially symmetric, unsteady, LES, and FW-H equations were solved by the implicit-time formulation. For the spatial discretization, second-order upwind scheme was employed. Dynamic mesh model also was applied to the ballistic domain which shifted with time. Results obtained for the muzzle flow field and for the far-field noise were compared with those obtained from experimental shadow photographs and measurements; these two batches of results were in agreement. Furthermore, the present computational predictions revealed clearly the detailed shock waves propagations/interactions inside the suppressor models and around the muzzle region. These results were detailed by the pressure time histories at recorded locations in each suppressor model as well as pressure contours and velocity vectors in the suppressor. It is noted that muzzle flows with species concentrations were also analyzed. The far-field noises, described by sound pressure levels (dB) and frequencies (Hz), generated by gunshots were also compared.

2. Mathematical Formulation and Numerical Method

2.1. Governing Equations

A gunshot generates complex physical phenomena, which involves chemical reactions induced by the discharged gases. This transient flow and acoustics are characterized by shock propagation, interaction, reflection, and disturbance around the muzzle and are affected by the species of propellant and structure of suppressors. Although the time duration of the present problem is very short, to calculate the noise generated by the pressure disturbance,

the viscous effects are considered. For the axisymmetric geometries, the continuity equation is given by

$$\frac{\partial \rho}{\partial t} + \frac{\partial}{\partial x}(\rho v_x) + \frac{\partial}{\partial r}(\rho v_r) \frac{\rho v_r}{r} = 0, \quad (2.1)$$

where x is the axial coordinate, r is the radial coordinate, v_x is the axial velocity, and v_r is the radial velocity. The axial, viscid flow is described in its conservation form by the Navier-Stokes equations. The equations of momentum and energy can be expressed as

$$\begin{aligned} \frac{\partial}{\partial t}(\rho v_x) + \frac{1}{r} \frac{\partial}{\partial x}(r \rho v_x v_x) + \frac{1}{r} \frac{\partial}{\partial r}(r \rho v_r v_x) &= -\frac{\partial p}{\partial x} + \frac{1}{r} \frac{\partial}{\partial x} \left[r \mu \left(2 \frac{\partial v_x}{\partial x} - \frac{2}{3} (\nabla \cdot \vec{v}) \right) \right] \\ &\quad + \frac{1}{r} \frac{\partial}{\partial r} \left[r \mu \left(\frac{\partial v_x}{\partial r} + \frac{\partial v_r}{\partial x} \right) \right] + F_x + S_m, \\ \frac{\partial}{\partial t}(\rho v_r) + \frac{1}{r} \frac{\partial}{\partial x}(r \rho v_x v_r) + \frac{1}{r} \frac{\partial}{\partial r}(r \rho v_r v_r) &= -\frac{\partial p}{\partial r} + \frac{1}{r} \frac{\partial}{\partial x} \left[r \mu \left(2 \frac{\partial v_r}{\partial x} + \frac{\partial v_x}{\partial r} \right) \right] \\ &\quad + \frac{1}{r} \frac{\partial}{\partial r} \left[r \mu \left(2 \frac{\partial v_r}{\partial r} + \frac{2}{3} (\nabla \cdot \vec{v}) \right) \right] - 2\mu \frac{v_r}{r^2} + \frac{2}{3} \frac{\mu}{r} (\nabla \cdot \vec{v}) \\ &\quad + \rho \frac{v_r^2}{r} + F_r + S_m, \\ \nabla \cdot \vec{v} &= \frac{\partial v_x}{\partial x} + \frac{\partial v_r}{\partial r} + \frac{v_r}{r}, \end{aligned} \quad (2.2)$$

where p is the static pressure, $\rho \vec{g}$ and \vec{F} are the gravitational body force and external body force, respectively. Note that E is the total energy and is defined as

$$\frac{\partial}{\partial t}(E) + \nabla(\vec{v}(E + p)) = -\nabla \left(\sum_j h_j J_j \right) + S_h, \quad (2.3)$$

where $\nabla(\sum_j h_j J_j)$ is the transport term of enthalpy due to species diffusion, and S_h is the term defined as the blast source term.

2.2. Numerical Method

The present numerical code utilizes the cell-averaged finite volume method. Considering the viscous effects, the large Eddy simulation (LES) turbulence model is used to resolve the large vortex structures in this study. In spatial discretization, the heat flux term is calculated by method of central difference. The quantities at cell faces are determined by assuming that the cell-center values of any field variable represent a cell-average value and hold throughout the entire cell; the face quantities are identical to the cell quantities. Thus the face value ϕ^i is set equal to the cell-center value of a scalar quantity ϕ in the upstream cell. The upwind

scheme with the flux, which the above-mentioned governing equations, of a cell's interface is presented as

$$\begin{aligned} \phi^i = & \frac{1}{2} \left(\phi^i(U_L) + \phi^i(U_R) \right) - \frac{1}{2} |\hat{\phi}| (U_R - U_L) = \frac{1}{2} \left(\phi^i(U_L) + \phi^i(U_R) \right) \\ & - \frac{1}{2} \hat{R}(\hat{U}) |\hat{\Lambda}| \hat{R}^{-1}(\hat{U}) (U_R - U_L), \end{aligned} \quad (2.4)$$

where U_L and U_R are the conservative variables at left and right sides of the cell interface, respectively. $\phi^i(U_L)$ and $\phi^i(U_R)$ are for calculating the flux between two sides of cell interface. $|\hat{\phi}|$ is a Jacobian matrix of $\phi(U)$, and $\hat{R}(\hat{U})$ is the right characteristic matrix of $|\hat{\phi}|$. $|\hat{\Lambda}|$ is a diagonal matrix that consists of characteristic lines. The characteristic velocities are $\hat{u}_q - \hat{c}$, \hat{u}_q , and $\hat{u}_q + \hat{c}$, where " $\hat{\cdot}$ " means the value calculated by Roe's average formula. Cell interface value is obtained by using second-order accuracy of the extrapolation method. The cell interface value is determined from the extrapolation method using a second-order weighted approximation, that is,

$$\begin{aligned} Q_{i+(1/2)}^L &= Q_i + \frac{1}{2} \delta Q_i, \\ Q_{i-(1/2)}^R &= Q_i - \frac{1}{2} \delta Q_i, \end{aligned} \quad (2.5)$$

where

$$\begin{aligned} \delta Q_j &= \text{ave}(Q_j - Q_{j-1}, Q_{j+1} - Q_j) \\ \text{ave}(a, b) &= \begin{cases} \min\text{mod}(a, b), & ab > 0 \\ 0, & ab < 0. \end{cases} \end{aligned} \quad (2.6)$$

For transient simulations, temporal discretization involved the integration of every term in the differential equations over a time step. Considering as unconditionally stable with respect to time step size, the fully implicit scheme was used in this study [22]. A generic expression for the time evolution of a variable ϕ is given by

$$\frac{\partial \phi}{\partial t} = F(\phi), \quad (2.7)$$

where the function F incorporates any spatial discretization. The implicit time integration of the transient terms was used, and the first-order backward difference used in accurate temporal discretization is given as

$$\frac{\phi^{n+1} - \phi^n}{\Delta t} = F(\phi^{n+1}), \quad (2.8)$$

where ϕ is scalar quantity, n and $n + 1$ are values at the current and next time levels, t and $t + \Delta t$, respectively,

$$\phi^{n+1} = \phi^n + \Delta t F(\phi^{n+1}). \quad (2.9)$$

This implicit equation can be solved iteratively by initializing ϕ^i to ϕ^n and iterating the equation given by

$$\phi^i = \phi^n + \Delta t F(\phi^i). \quad (2.10)$$

2.3. Moving Mesh Conservation Equations

In this study, the moving mesh model [23, 24] was employed in the movement of bullet during gunshot simulations. Upon release, the bullet moves as a result of the pressure differential; the six degree of freedom was used to compute this coupled motion, and the layering scheme [25] from the dynamic mesh (DM) model was utilized. The integral form of the conservation equation for a general scalar, ϕ , on an arbitrary control volume, V , whose boundary was moving, can be written as

$$\frac{d}{dt} \int_V \rho \phi dV + \int_{\partial V} \rho \phi (\vec{u} - \vec{u}_g) \cdot d\vec{A} = \int_{\partial V} \Gamma \nabla \phi \cdot d\vec{A} + \int_V S_\phi dV, \quad (2.11)$$

where ρ is the fluid density, \vec{u} is the flow velocity vector, \vec{u}_g is the grid velocity of the moving mesh, Γ is the diffusion coefficient, and S_ϕ is the source term of ϕ .

Here, dV is used to represent the boundary of the control (cell) volume V . The time derivative term in (2.11) can be made discrete and written by using a first-order backward difference formula as

$$\frac{d}{dt} \int_V \rho \phi dV = \frac{(\rho \phi V)^{n+1} - (\rho \phi V)^n}{\Delta t}, \quad (2.12)$$

where n and $n + 1$ denote the respective quantities at the current and next time steps. The volume V^{n+1} at the $(n + 1)$ th time step is computed from

$$V^{n+1} = V^n + \frac{dV}{dt} \Delta t, \quad (2.13)$$

where dV/dt is the time derivative of the control volume. In order to satisfy the grid conservation law, the time derivative of the control volume is computed from

$$\frac{dV}{dt} = \int_{\partial V} \vec{u}_g \cdot d\vec{A} = \sum_j^{n_f} \vec{u}_{g,j} \cdot \vec{A}_j, \quad (2.14)$$

where n_f is the number of faces on the control volume and \vec{A}_j is the j th face area vector. The dot product $\vec{u}_{g,j} \cdot \vec{A}_j$ on each control volume face is calculated from

$$\vec{u}_{g,j} \cdot \vec{A}_j = \frac{\delta V_j}{\Delta t}, \quad (2.15)$$

where δV_j is the volume swept out by the control volume face j over the time step Δt .

The dynamic mesh model, a six degree of freedom solver, was used to model flows where the shape of the domain changed with respect to the motion on the obstacle boundaries. Translational and angular motions of the center of gravity were calculated from the object's forces and moments balance on a solid body. The governing equation for the translational motion of the center of gravity was solved for in the inertial coordinate system:

$$\dot{\vec{v}}_G = \frac{1}{m} \sum \vec{f}_G, \quad (2.16)$$

where $\dot{\vec{v}}_G$ is the translational motion of the center of gravity, m is the mass, and \vec{f}_G is the force vector due to the gravity.

The angular motion of the object, $\dot{\vec{\omega}}_B$, is computed using the body coordinates

$$\dot{\vec{\omega}}_B = L^{-1} \left(\sum \vec{M}_B - \vec{\omega}_B \times L \vec{\omega}_B \right), \quad (2.17)$$

where L is the inertia tensor, \vec{M}_B is the moment vector of the body, and $\vec{\omega}_B$ is the rigid body angular velocity vector. The moments are transformed from inertial to body coordinates using

$$\vec{M}_B = R \vec{M}_G, \quad (2.18)$$

where R is the transformation matrix and is expressed as follows:

$$\begin{bmatrix} C_\theta C_\varphi & C_\theta C_\varphi & -S_\theta \\ S_\phi S_\theta C_\varphi - C_\phi S_\varphi & S_\phi S_\theta S_\varphi - C_\phi C_\varphi & S_\phi C_\theta \\ C_\phi S_\theta C_\varphi - S_\phi S_\varphi & C_\phi S_\theta S_\varphi - S_\phi C_\varphi & C_\phi C_\theta \end{bmatrix}, \quad (2.19)$$

where, in generic terms, $C_x = \cos(x)$ and $S_x = \sin(x)$. The angles ϕ, θ , and φ are Euler angles that represent the rotations along x -, y -, and z -axes, respectively. The angular and translational velocities were used in the dynamic mesh calculations to update the physical values at the mesh points. Once the angular and the translational accelerations are computed from (2.16) and (2.17), both velocities are derived by numerical integration and are used in the dynamic mesh calculations to update the rigid body position.

In the process of dynamic computation, to achieve better computational quality, the nondeformable fitted meshes in the front and rear regions of the bullet were modeled. And the other meshes along trajectory (interface region) were constructed with uniform structure meshes. By using moving mesh model, the boundary conditions on both ends of chamber and trajectory were assumed unmovable. Additionally, mesh sizes on both ends could be

adjusted with the interface region moving, as shown in Figure 3. On the left side, the meshes were enlarged until reaching the limited size which is one-and-half-times larger than the original size. Otherwise, the meshes would be compressed until the size is less than half of the original size. Multiblock, conformal, unstructured meshes (adjoined to the projectile and in suppressor), and uniform meshes along the moving trace were adopted. The other domain was employed for the structure meshes with stretching distribution. The gunshot simulation involved a total of 500,000 cells.

2.4. Acoustic Analogy Model

The main challenge in numerically predicting the sound waves stems from the fact that the sounds have much lower energy than fluid flows. Another challenge is the difficulty of predicting the various flow phenomena (e.g., turbulence) in the near field that generates sounds. In this study, an attempt was made to predict both the flow field and emitted sound of gunshot in far field. Owing to the supersonic flow field, the equations were solved on the basis of compressibility. The present simulation was attempted to capture this flow field by LES turbulence model with moving mesh system. The sound propagation was calculated also by the Ffowcs-Williams and Hawkings analogy [26], as shown in Figure 4. Although expending more computing source, LES turbulence model was applied in the prediction of the pressure fluctuations. The mechanism of the aerodynamic noise radiation is revealed. The noise is mainly radiated from the muzzle and bullet, generating strong vortices and shock.

The Ffowcs Williams and Hawkings equation adopted Lighthill's acoustic analogy to predict the sound generated by the acoustic sources from muzzle blast. The FW-H equation is given by

$$\begin{aligned} \frac{1}{a_0^2} \frac{\partial^2 p'}{\partial t^2} - \nabla^2 p' &= \frac{\partial^2}{\partial x_i \partial x_j} \{T_{ij} H(f)\} - \frac{\partial}{\partial x_i} \{ [P_{ij} n_j + \rho u_i (u_n - v_n)] \delta(f) \} \\ &+ \frac{\partial}{\partial t} \{ [\rho_0 v_n + \rho (u_n - v_n)] \delta(f) \}, \end{aligned} \quad (2.20)$$

where u_i and v_i are fluid velocity components in the x_i direction. u_n and v_n are normal to the surface $f = 0$. $\delta(f)$ is Dirac delta function and $H(f)$ is Heaviside function. p' is sound pressure at the far field and is presented as: $p' = p - p_0$,

$$\begin{aligned} T_{ij} &= \rho u_i u_j + P_{ij} - a_0^2 (\rho - \rho_0) \delta(f), \\ P_{ij} &= p \delta_{ij} - \mu \left[\frac{\partial u_i}{\partial x_j} + \frac{\partial u_j}{\partial x_i} - \frac{2}{3} \frac{\partial u_k}{\partial x_k} \delta_{ij} \right]. \end{aligned} \quad (2.21)$$

3. Comparisons of Numerical Algorithms with Experimental Results

3.1. Shock Structure of Muzzle Flow

To compare the muzzle flow structures, numerical simulation was completed by the experimental shadowgraph [27]. The schematic flow evolutions outside the barrel were calculated over a 1.5 ms time interval, as shown in Figure 5. The barrel shock was modeled, but with

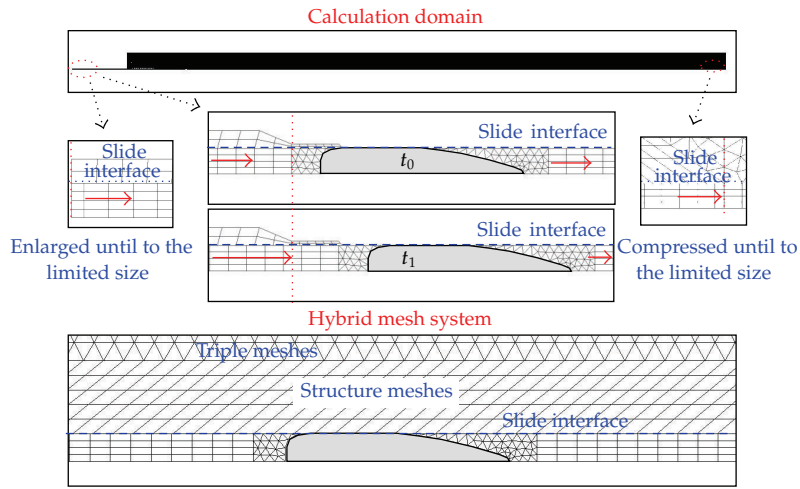


Figure 3: Description of generation of moving grids.

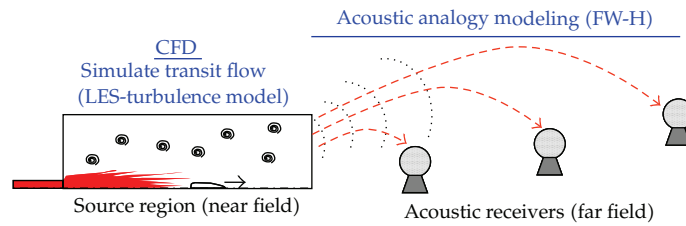


Figure 4: Schematic illustration of acoustic analogy model.

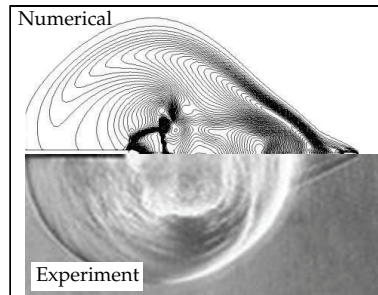


Figure 5: Comparison of muzzle flow structures between numerical simulation isopycnics and experimental results [27].

a slightly different shape than that of the experimental data. The barrel shock with free-shear layer, vortex structure, and the slipstream were modeled with this CFD simulation.

3.2. Gunshot Noises Comparison

Numerical acoustic predictions of gunshot of a 7.62 mm rifle were simulated, and comparison of numerically obtained results with those obtained experimentally [28] was in agreement.

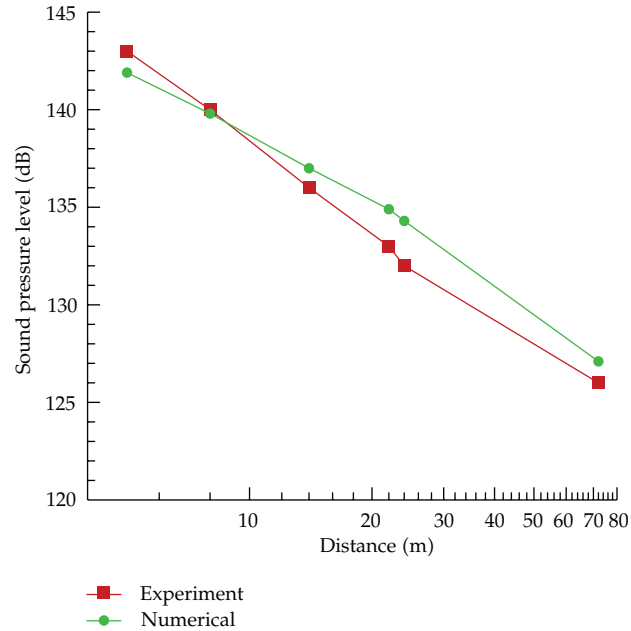


Figure 6: Comparisons of peaks of sound pressure level (dB) between numerical and experimental results [28].

In this simulated case, the air with high pressure (200 atm) and temperature (1500°K) in chamber generates the bullet with a velocity of 840 m/s at muzzle. The peaks of sound pressure levels were recorded at different locations behind muzzle, with the distances located at 5 m, 8 m, 12 m, 22 m, 24 m, and 72 m from the muzzle. The comparisons of peak of sound pressure level (dB) between numerical and experimental results are shown in Figure 6, and the differences are within 2 dB. In this study, excellent agreements among the computational results and the experimental results were achieved.

4. Results and Discussions

In this study, a bullet was initially resting adjacent to the chamber where the pressure and temperature were patched up to 200 atm and 1500°K , while the ambient air pressure and temperature were 1 atm and 300°K , respectively. Five cases, which include one case with a rifle unsuppressed and four cases with a suppressed rifle, were simulated by solving the finite volume method for axial-symmetric, compressible, unsteady, viscous flow.

4.1. Illustration of Geometry

A schematic illustration of different suppressors and boundary conditions is displayed in Figure 7. The chamber, bullet, barrel, and suppressor were assumed to be nonslip and with isotherm rigid surfaces. The inner diameter of the tubular sleeves is 4 cm, total length of tubular body is 15 cm, and the length of barrel is 50 cm. The domain of calculation is $4\text{ m} \times 0.5\text{ m}$ (length \times height). The boundary condition of the trajectory, which was the path of

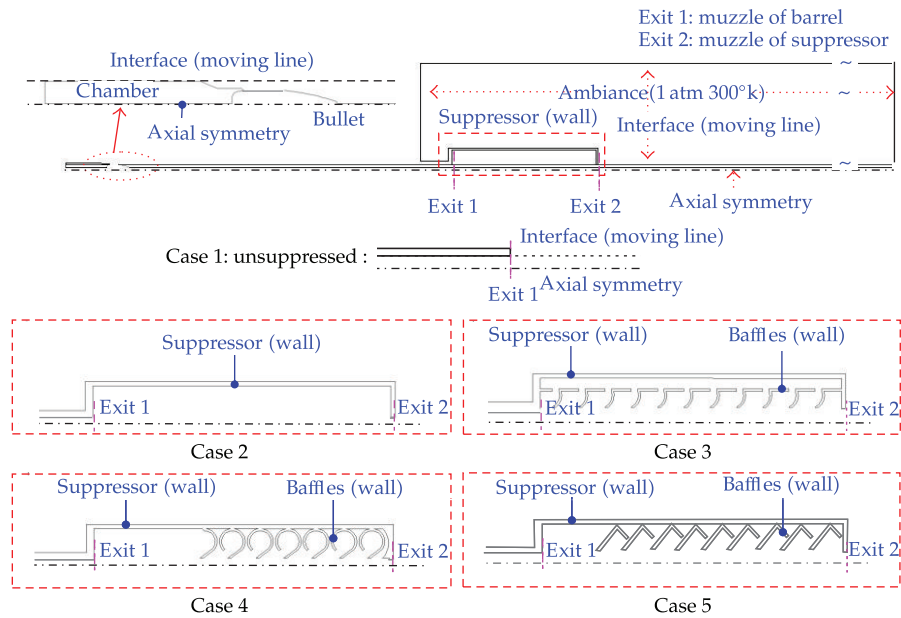


Figure 7: Schematic diagrams of different suppressors and boundary conditions.

a bullet moving, was set as an interface condition for dividing the regions between trajectory and barrel, and trajectory and ambiance. On the other side, the boundary condition for the central line was set as axially symmetric.

4.2. Shock Wave Structures of Muzzle Flow Field by Species Distribution

Series images of species distributions of muzzle flow field in Case 1 with gunshot of unsuppressed rifle are displayed in Figure 8. The development of flow structure includes jet flow, propagations, interactions, collisions, dissipation, and vortex, displayed at 0.82, 1.0, 1.5, 2.0, 2.5, and 3.0 ms. The high-pressure and -temperature gas ejected from the barrel, expanded radially, and formed a typical jet flow structure, as shown in Figure 8(a). However, the obstruction by the axially moving bullet caused the ejecting angle to be larger than the typical muzzle jet flow at muzzle region. Besides, the strong discharged gas interacted with the ambient air and generated disturbance and vortex which caused the noise, as shown in Figures 8(b)–8(f). Subsequently, the bullet moved away from muzzle; the jet flow still injected and interacted with surrounding air until its strength scattered.

There are four kinds of suppressors simulated with the same dimension (length and diameter) in this study. In Case 2–Case 5, at 0.82 ms, discharged gas flowed into the space of suppressors when the bullet was at the exit of suppressor, as shown in Figure 9(a). It is noted that the tube-shaped suppressor of Case 2 (without any obstacle inside the suppressor) was almost full of discharged gas. While the bullet traveled out of suppressor, large amount of gas was discharged from suppressor. Owing to the design of suppressor, both suppressors in Case 2 and Case 3 (which arranged serial of even chambers) generated more species gases at 1.00 ms, as shown in Figure 9(b)s. At 2 ms and 3 ms, the jet flow was ejected along axial

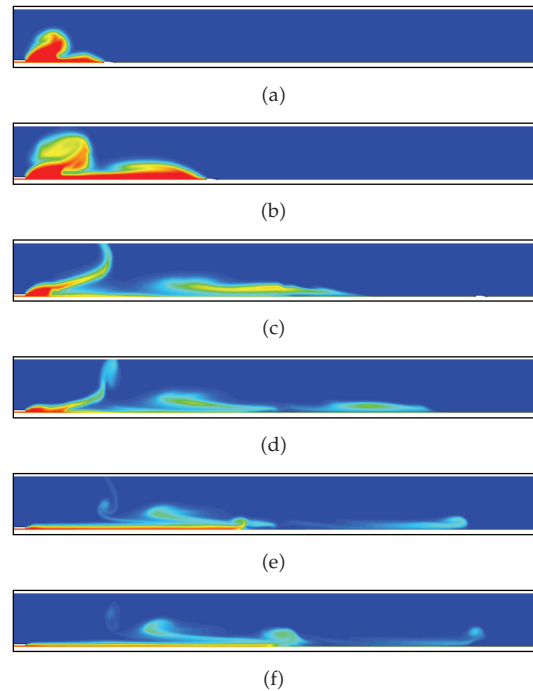


Figure 8: Series numerical images of species distributions near muzzle region by the gunshot of unsuppressed rifle in Case 1: (a) 0.82 ms, (b) 1.0 ms, (c) 1.5 ms, (d) 2.0 ms, (e) 2.5 ms, and (f) 3.0 ms.

direction for all cases under study. There is more discharged gas in the barrel and suppressor regions for Case 4 and Case 5 than that for the other cases, as shown in Figure 9(c)s and 9(d)s. In addition, disturbance phenomena were found near 0.5 m for muzzle in Case 4 which were caused by an uneven ejection of discharged gas, as shown in Figure 9(c)s.

4.3. Shock Wave Structures in Suppressors and Muzzle Flow Field

For each image of Figure 10, the velocity vectors (up) and pressure contours (down) of unsuppressed rifle during gunshot are presented. Serials of images are presented from 0.68 ms to 0.88 ms with 0.04 ms interval. At 0.68 ms, the accelerating bullet was compressing the air in gun tube, forming the first precursor shock in the muzzle, as shown in Figure 10(a). After the bullet has passed through muzzle, as shown in Figures 10(b) and 10(c), the high-pressure and -temperature air was discharged, followed by the bullet. The interaction between high-speed bullet and surrounding air formed a shock wave, attached on the bullet at 0.72 ms. The muzzle jet propagated radially and produced a typical bulk shock structure. The flow was construed (constructed) by several characteristics of muzzle-jet flow such as jet boundary, main shock, and vortex, as shown in Figure 1. In fact, the disturbance around muzzle was the source of noise and its power in this case was larger than that in the other cases. As the jet flow was propagating farther, the jet flow along the axial direction interacted with the side jet flow and caused the local flow to move in the opposite direction, as shown in Figures 10(d)–10(f). The interaction increased the friction of air and caused larger noise. Besides, the location of the shock wave also expanded and moved outward from the muzzle.

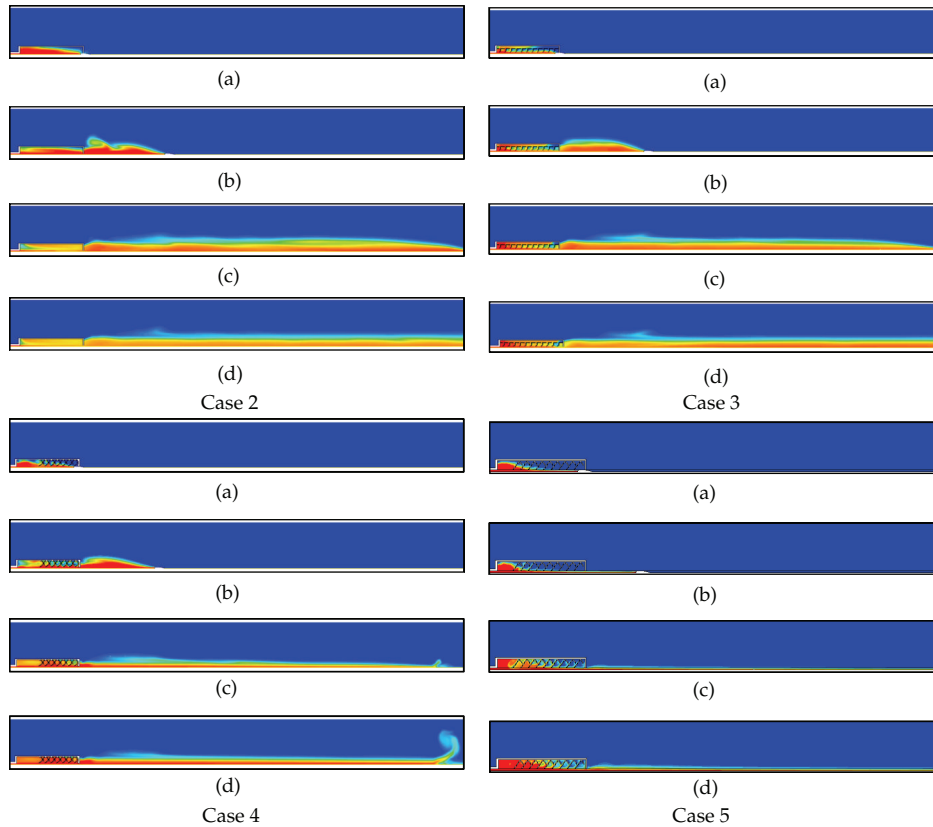


Figure 9: Series numerical images of species distributions near muzzle region by the gunshot of suppressed rifle in Case 2–Case 5: (a) 0.82 ms (b) 1.00 ms (c) 2.00 ms (d) 3.00 ms.

The suppressor was designed as a tube in Case 2. While the bullet was passing through muzzle and entering the suppressor, the precursor still moved in front of the bullet head and the discharged gas was ejected into the suppressor radically, forming a shock wave, as shown in Figure 11(a). At 0.80 ms, while the bullet was moving near the end of suppressor, the gas was almost full in this space, as shown in Figure 11(b). After the bullet has passed through the suppressor, the gas was ejected out and interacted with the ambient air. The air close to the muzzle of suppressor was pushed outward and a vortex was formed around its surface, as shown in Figure 11(c). Inside the suppressor, part of the gas was reflected from the wall, interacting with the incident gas and decreasing the impact of the jet. In Figure 11(d), the incident gas in suppressor still interacted with the reverse flow and delayed the exit flow of suppressor.

In Case 3, eleven sets of baffle plates divided the barrel space into two lengthwise levels and twelve small chambers in the suppressor. The jet flow traveled mainly along the central passage; part of the gas flowed into these small chambers and the outer space by the guidance of baffle plates and the obstruction of bullet, as shown in Figures 12(a) and 12(b). Besides, the flow impacted on the corners of baffle plate entrance; subsequently, the flow formed shocks and interacted symmetrically. While the bullet was passing through muzzle, the discharged gas was ejected outward and interacted with the surrounding air, forming

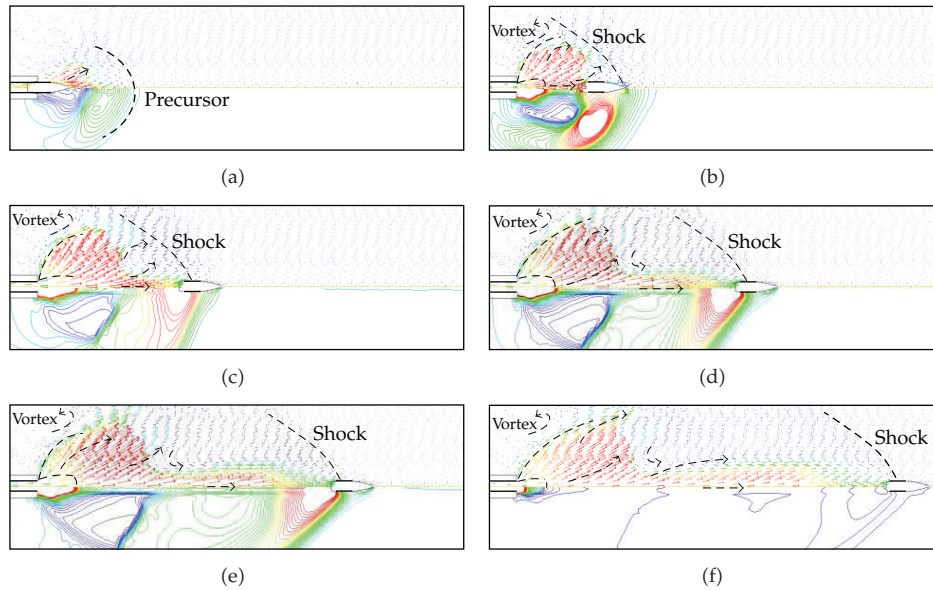


Figure 10: Distributions of pressure and velocity vectors in Case 1 (a) 0.68 ms (b) 0.72 ms (c) 0.76 ms (d) 0.80 ms (e) 0.84 ms (f) 0.88 ms.

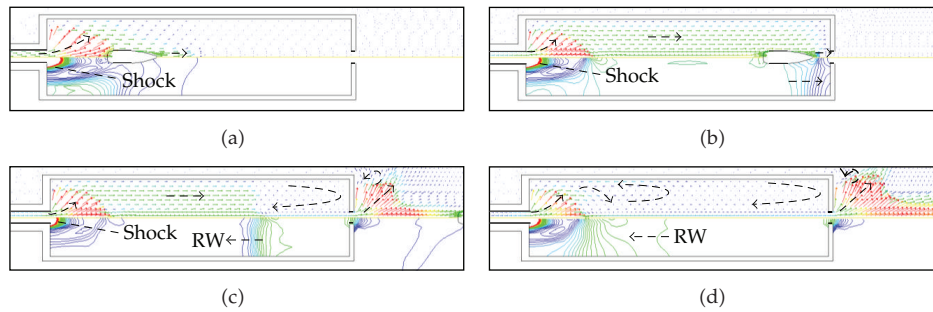


Figure 11: Distributions of pressure and velocity vectors in Case 2 (a) 0.72 ms, (b) 0.80 ms, (c) 0.86 ms, and (d) 0.90 ms.

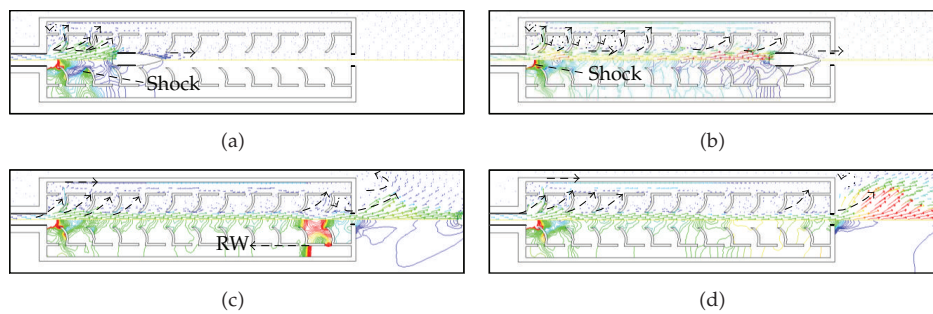


Figure 12: Distributions of pressure and velocity vectors in Case 3 (a) 0.72 ms, (b) 0.80 ms, (c) 0.86 ms, and (d) 0.90 ms.

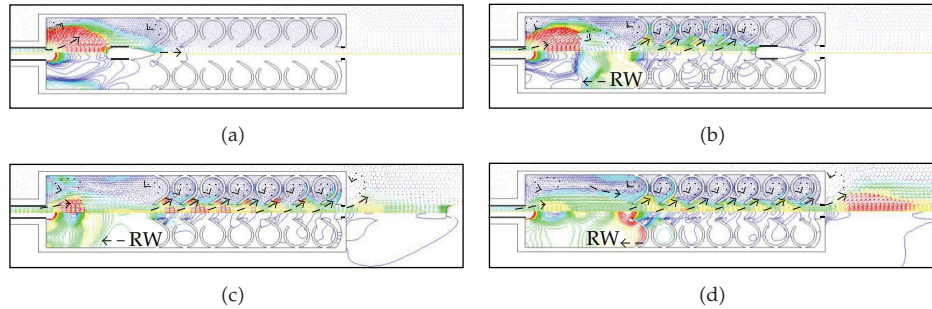


Figure 13: Distributions of pressure and velocity vectors in Case 4 (a) 0.72 ms, (b) 0.80 ms, (c) 0.86 ms, and (d) 0.90 ms.

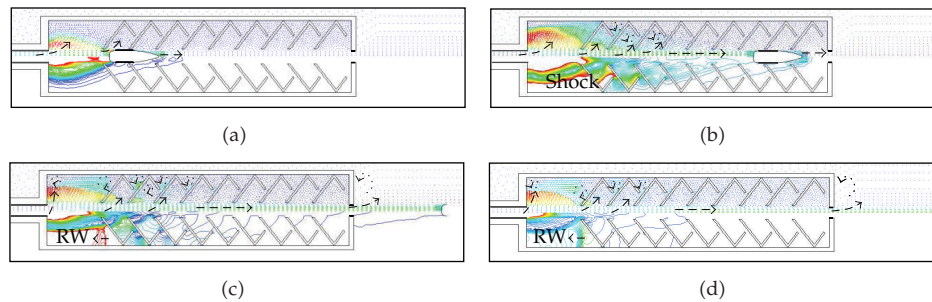


Figure 14: Distributions of pressure and velocity vectors in Case 5 (a) 0.72 ms, (b) 0.80 ms, (c) 0.86 ms, and (d) 0.90 ms.

a vortex out of the suppressor, as shown in Figures 12(c) and 12(d). Following the speedy movement of the bullet, the jet obstructed in the suppressor and ejected farther.

In Case 4, another structure of suppressor was combined with a larger space in the front section, and six small chambers were separated by six and one-half sets of baffle plates, as shown in Figure 13. The design of the front space was to mitigate the impact of discharged gas and to shift the noise frequency. In Figure 13(a), the air was pushed by the high-pressure discharged gas and was flowing backwards. When the bullet was traveling axially in the suppressor, the gas that followed was guided into the front and the other smaller chambers. The reversed flow was formed and further interacted with the incident jet flow, as shown in Figure 13(b). At 0.86 ms, as shown in Figures 13(c) and 13(d), the jet flow interacted with the air and generated a vortex near the suppressor. While the axial jet flow was colliding with these baffle plates, reflected shocks were generated and the incident flow was protracted, as in Case 4.

The design and flow characteristics of suppressor in Case 5 were similar to those in Case 4. A larger space in the front section and nine sets of V-shaped baffle plates forming small chambers, as shown in Figure 14. The front section provided the mitigating space, thus the discharged gas interacted with the first set of baffle plates of suppressor and became stagnant for a while, as shown in Figure 14(a). Although the V-shaped baffle plates were different from the curved ones used in Case 4, the eliminating effects resulting from the reversed flow in various chambers were similar. Except for the fact that the direction of

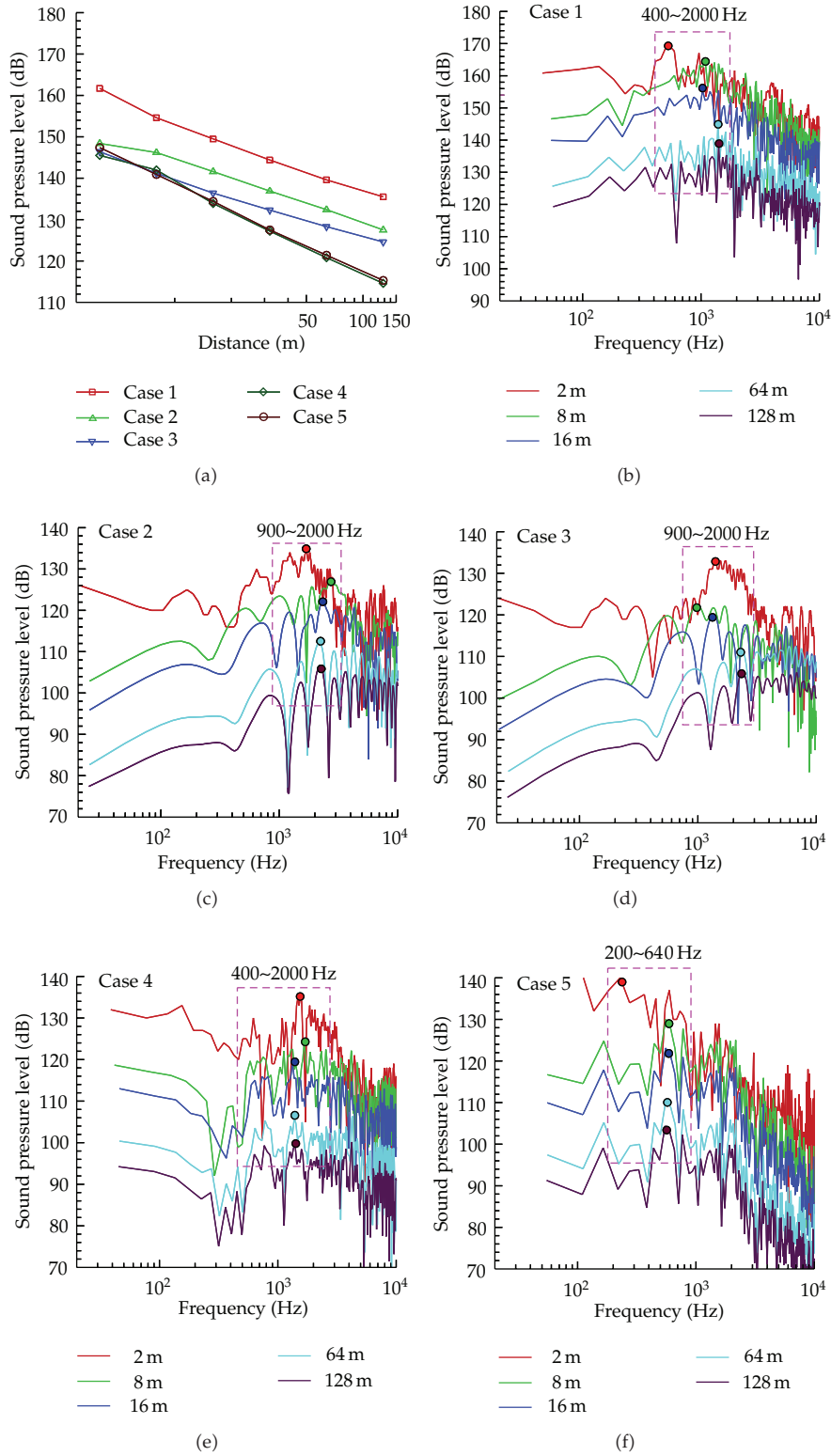


Figure 15: Comparison of sound pressure level (a) and spectral analysis of pressure signals ((b)-(f)).

reverse flow in the front space was different, the flow structures in the suppressor for Case 5 were also similar to those for Case 4, as shown in Figures 14(c) and 14(d).

4.4. Comparison of Noise with Different Suppressors

In this study, the Ffowcs Williams and Hawkings acoustics were modeled to calculate the far-field sound signals. The acoustic pressure signals were also post-processed by the fast Fourier transform (FFT). The effects of noise attenuation in Case 4 and Case 5 were lower (16 dB at 4 m and 20 dB at 128 m) than those in Case 1 (the case with no suppressor attached), as shown in Figure 15(a). In fact, suppressor with an expansion chamber (Case 2) or suppressors with a series of the baffle plates (Case 3–Case 5) attached on the barrel could reduce the first peak pressure at the exit of the exhaust pipe. In this study, the sound pressure levels were different for various assigned receivers at logistic lengths from 4 m to 128 m. The sound pressure level (dB) in Case 1 showed higher peaks and were centralized in 400–2000 Hz, as shown in Figure 15(b). While an expansion chamber was attached to the rifle in Case 2, the sound pressure levels were reduced, as shown in Figure 15(c). Figure 15(d) demonstrates that the baffles arranged in the chamber of suppressor really decrease the noise. In Case 4 and Case 5, arrangements in the chambers were responsible for causing the shock waves to cancel one another, resulting in a reduction in noise. Besides, the sensitive region (which is around 1,000–3,000 Hz) of noise frequencies is avoided by these designs of baffles, as shown in Figures 15(e) and 15(f).

5. Conclusions

The aim of this study was to investigate the time-dependent turbulent flow associated with the blast wave which originates from rifle shooting. Sound sources were also evaluated during the flow calculation, together with the calculation of the acoustic signals for different receivers. The impulse noise methodology was employed to analyze and compare the noise attenuation properties of suppressors. Actually, these attenuated effects must be evaluated against the risk of hearing damage in the vicinity of these noise impulses and against disturbances farther away.

In this study, the muzzle flow field and noise of rifle shooting were validated with experimental results. In addition, the SPL (dB) were also compared in far field among the rifles equipped with different suppressors. The LES and species transport models were useful to provide the acoustic source. The FW-H model was also useful to calculate SPL in far field. Changing the shapes, numbers, and volumes of chambers in limited size of suppressor could shift the frequency and decrease the noise in gunshot. It is difficult to obtain absolute SPL predictions in 2D or axial domain due to the need to estimate the correlation length of the turbulent flow structures in the spanwise direction. The proposed physical model and the numerical simulations used in the present work can be extended to solve other weapon shooting problems with three-dimensional and complex geometries.

References

- [1] G. Klingenberg, "Gun muzzle blast and flash," *Propellants, Explosives, Pyrotechnics*, vol. 14, no. 2, pp. 57–68, 1989.
- [2] J. C. T. Wang and G. F. Widhopf, "Numerical simulation of blast flowfields using a high resolution TVD

- finite volume scheme," *Computers and Fluids*, vol. 18, no. 1, pp. 103–137, 1990.
- [3] G. Klingenberg and G. A. Schröder, "Investigation of combustion phenomena associated with the flow of hot propellant gases-II: gas velocity measurements by laser-induced gas breakdown," *Combustion and Flame*, vol. 27, no. C, pp. 177–187, 1976.
 - [4] R. C. Maher, "Modeling and signal processing of acoustic gunshot recordings," in *Proceedings of the 12th Digital Signal Processing Workshop (DSP '06)*, pp. 257–261, Jackson Lake, Wyo, USA, 2006.
 - [5] R. C. Maher, "Acoustical characterization of gunshots," in *Proceedings of the Signal Processing Applications for Public Security and Forensics, (SAFE '07)*, Washington, DC, USA, 2007.
 - [6] B. E. Koenig, S. M. Hoffman, H. Nakasone, and S. D. Beck, "Signal convolution of recorded free-field gunshot sounds," *Journal of the Audio Engineering Society*, vol. 46, no. 7, pp. 634–651, 1998.
 - [7] G. L. Duckworth, D. C. Gilbert, and J. E. Barger, "Acoustic counter-sniper System," in *Proceedings of SPIE Command, Control, Communications, and Intelligence Systems for Law Enforcement*, vol. 2938, pp. 262–275, 1997.
 - [8] G. S. Settles, T. P. Grumstrup, J. D. Miller, M. J. Hargather, L. J. Dodson, and J. A. Gatto, "Full-scale high-speed "Edgerton" retroreflective shadowgraphy of explosions and gunshots," in *Proceedings of the 5th Pacific Symposium on Flow Visualization and Image Processing (PSFVIP '05)*, Australia, 2005.
 - [9] D. L. Cler, N. Chevaugeron, M. S. Shephard, J. E. Flaherty, and J. F. Remacle, "Computational fluid dynamics application to gun muzzle blast—a validation case study," Tech. Rep. ARCCB-TR-03011, 2003.
 - [10] M. K. Hudson, C. Luchini, J. K. Clutter, and W. Shyy, "CFD approach to firearms sound suppressor design," *American Institute of Aeronautics and Astronautics*, pp. 96–3020, 1996.
 - [11] R. Pääkkönen, "Noise attenuation of structures against impulses from large calibre weapons or explosions," *Applied Acoustics*, vol. 45, no. 3, pp. 263–278, 1995.
 - [12] A. Paulson and N. R. Parker, "5.56 mm Suppressors for the M16A1," *The Small Arms Review*, vol. 5, no. 8, pp. 83–89, 2002.
 - [13] L. W. Grau and C. Q. Cutshaw, "Russian snipers in the mountains and cities of Chechnya," *Infantry*, vol. 7, pp. 7–11, 2002.
 - [14] R. Pääkkönen, "Environmental noise reduction means of weapons," *Acoustic*, pp. 5811–5814, 2008.
 - [15] B. J. Boersma and J. M. Burgerscentre, "Numerical simulation of the noise generated by a low Mach number, low Reynolds number jet," *Fluid Dynamics Research*, vol. 35, no. 6, pp. 425–447, 2004.
 - [16] S. Sarkar, M. Y. Hussaini et al., "Computation of the sound generated by isotropic turbulence," NASA Contract Report 93-74, NASA Langley Research Center, Hampton, VA, USA, 1993.
 - [17] M. Wang, J. B. Freund, and S. K. Lele, "Computational prediction of flow-generated sound," *Annual Review of Fluid Mechanics*, vol. 38, pp. 483–512, 2006.
 - [18] A. D. Khondge, S. D. Sovani, S. E. Kim, A. A. Farag, and S. C. Guzy, "On predicting the aeroacoustic performance of ducts with broadband noise source models," SAE Paper 2005-01-2495, 2005.
 - [19] Y. Wang, Z. Gu, W. Li, and X. Lin, "Evaluation of aerodynamic noise generation by a generic side mirror," in *Proceedings of the World Academy of Science, Engineering and Technology*, vol. 61, pp. 364–371, 2010.
 - [20] V. Kannan, S. D. Sovani, D. Greeley, and A. Khondge, "Computational aeroacoustics simulation of whistle noise in an automotive air-intake system," SAE International 2005-01-2364, 2005.
 - [21] M. J. Lighthill, "On sound generated aerodynamically," in *Proceedings of the Royal Society. Series A*, pp. 564–587, London, UK, 1952.
 - [22] C. Hirsch, *Numerical Computation of Internal and External Flow*, vol. 2 of *Computational Methods for Inviscid and Viscous Flows*, Wiley, New York, NY, USA, 1992.
 - [23] D. O. Snyder, E. K. Koutsavdis, and J. S. R. Anttonen, "Transonic store separation using unstructured CFD with dynamic meshing," Tech. Rep. 2003-3913, AIAA, 2003.
 - [24] J. K. Jordan, N. E. Suhs, R. D. Thoms, R. W. Tramel, J. H. Fox, and J. C. Erickson, "Computational time-accurate body movement methodology, validation, and application," AEDC-TR-94-15, 1995.
 - [25] R. Koomullil, G. Cheng, B. Soni, R. Noack, and N. Prewitt, "Moving-body simulations using overset framework with rigid body dynamics," *Mathematics and Computers in Simulation*, vol. 78, no. 5-6, pp. 618–626, 2008.
 - [26] J. E. Ffowcs-Williams and D. L. Hawkins, "Sound generation by turbulence and surfaces in arbitrary motion," in *Proceedings of the Royal Society. Series A*, vol. 264, no. 1151, pp. 321–342, London, UK, May 1969.
 - [27] G. Settles, "High-speed imaging of shock waves, explosions and gunshots," *American Scientist*, vol. 94, no. 1, pp. 22–31, 2006.
 - [28] Department of the U.S. Army, "Data Base for Assessing the Annoyance of the Noise of Small Arms," Technical Guide 135, HSHB-OB/WP, 1983.